A phase-based method for measuring local convective heat transfer coefficients

William Davis[*], Nicholas R. Atkins

Whittle Laboratory, Department of Engineering, University of Cambridge, Cambridge, UK

Abstract

Existing experimental heat transfer coefficient measurement techniques rely on the amplitude of the wall temperature, making the coefficients sensitive to noise and limited in spatial resolution. This paper presents a novel measurement technique that uses the phase-shift between wall and fluid temperatures to measure convective heat transfer coefficients. Here the phase-based method is derived theoretically, analysed numerically and validated experimentally with comparison to an existing transient technique. It is shown that using phase-shift rather than amplitude reduces a heat transfer coefficient measurement's sensitivity to noise by a factor of 10-50, reducing the power requirements for an experiment and enabling high spatial resolution measurements.

Keywords:
heat transfer coefficient, phase-based measurement, infrared thermography

Nomenclature

Roman Symbols

Bi	Biot number
Fo	Fourier number
H	Step height
L	Characteristic length
M	Mach number
Nu	Nusselt number
Re	Reynolds number
T	Temperature
e	Thermal effusivity
f	Frequency
h	Heat transfer coefficient
j	Imaginary unit
$\dot{q}$	Heat flux
s	Laplace parameter
t	Time
x	Stream-wise coordinate
y	Wall-normal coordinate

Greek Symbols

Θ	Temperature difference parameter
α	Thermal diffusivity
δ	Error term
λ	Thermal conductivity
ϕ	Phase
ω	Angular frequency

Subscripts

∞	Free stream value
N	N^{th} harmonic value
aw	Adiabatic wall value
i	Initial value
lim	Limiting value
n	Noise value
w	Wall value

Other Symbols

$\frown$	Laplace transformed variable

Abbreviations

CW	Cold-Wire
IR	InfraRed
SNR	Signal-to-Noise Ratio
TC	ThermoCouple

1. Introduction

When designing thermally-limited components local quantities must be captured to identify hot spots that constrain component life. While computational methods for calculating heat loads have advanced, there remains a need for experimental methods to capture physics that simulations cannot. This paper focuses on measuring heat transfer coefficients in flows with forced convection. We define a locally invariant heat transfer coefficient h, relative to the heat flux through the wall $\dot{q}$, as

$$\dot{q} = -\lambda \frac{\partial T(y)}{\partial y}\bigg|_{y=0} = h(T_{\text{aw}} - T_{\text{w}}) \tag{1}$$

where the solid has thermal conductivity λ and a temperature profile T relative to the coordinate y, which is normal and into the wall. The wall has temperature T_{w}, such that $T(0) = T_{\text{w}}$, and T_{aw} is the temperature of the wall if there were no heat transfer. T_{aw} is determined by the total temperature, Mach number and recovery factor of the flow. Moffat [1] explains that using T_{aw} as the reference temperature makes h largely independent of the wall temperature, resulting in a purely aerodynamic parameter.

[*]Corresponding author
Email address: wd269@cam.ac.uk (William Davis)

For cases with strong coupling between the fluid and wall temperatures other formulations for heat transfer exist, such as the spectral heat transfer coefficient proposed by He [2] and the discrete Green's function method proposed by Hacker and Eaton [3]. These formulations are not widely used and so are not addressed in this paper.

Experimental measurement methods based on transient temperature changes usually measure the amplitude response of T_w to calculate h from a fit to the governing equations. A major source of error in this method is noise in the wall temperature measurement. With fixed instrumentation noise this error is minimised by maximising the temperature difference to be measured (the signal), thereby increasing the signal-to-noise ratio (SNR). In rigs with high mass flows, such as a turbine, the heating or cooling power required to generate a usable temperature difference quickly becomes impractical.

This paper presents a novel method of measuring local heat transfer coefficients by measuring the phase-shift between T_{aw} and T_w when T_{aw} is varied periodically. It is demonstrated that measuring phase-shift rather than amplitude reduces the sensitivity to noise by a factor between 10 and 50. This enables a corresponding decrease in the power input to an experiment, allowing for practical testing of real components.

The paper is split into five parts:

- Current practice in measuring local heat transfer coefficients and past work on phase-based methods is reviewed.
- Theory for the new phase-based method is developed.
- Numerical experiments are carried out to analyse the phase-based method and compare it to existing practice.
- Details of the method for experimental validation of the phase-based method are given.
- Results from validation experiments are presented and discussed with comparison to an existing method.

2. Literature review

This section reviews current practice on measuring local convective heat transfer coefficients. Thorough reviews of heat transfer measurement methods and instrumentation can be found in Refs. [4–6].

2.1. Current practice in heat transfer coefficient measurement

Here the literature is reviewed on common experimental methods for measuring heat transfer coefficients on semi-infinite walls. Two classes of experiment are discussed: steady state and transient.

Figure 1 illustrates how heat transfer coefficients are measured in current practice by generating a heat flux and measuring temperature response of the wall. Equation 1 shows that measurements of heat flux at multiple different wall temperatures allow a heat transfer coefficient to be calculated from the gradient of a linear regression line on the data. Wall temperature data can also be used in a regression to fit to governing equations other than Eq. 1. In an experiment some data will fall outside of the assumptions of the measurement. The range of wall temperatures for which assumptions hold and a fit can be achieved is referred to as the regression extent.

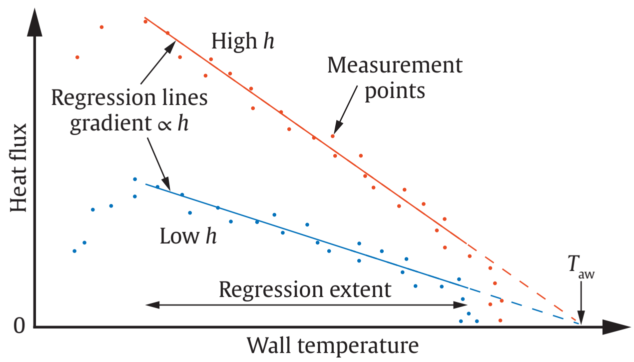

Figure 1 Illustration of a traditional heat transfer measurement using heat flux.

Steady state methods are performed in fixed aerothermal conditions. A constant heat flux is applied to a test piece and wall temperature measurements from tests with different heat flux values are used to calculate heat transfer coefficients. Laveau et al. [7] measured heat transfer coefficients on the end wall of a cascade with an isothermal copper back plate covered in a kapton insulator. Wall temperatures were measured with an infrared (IR) camera and heat flux was calculated by applying Fourier's law of conduction. Laveau et al. [7] estimated uncertainties in heat transfer coefficient of 13 %, with the main source of uncertainty being the conductivity of the insulating layer. Problems were also found with trapped air pockets in the insulator, showing the difficulties in applying this method to complex geometries. Another method uses a thin-foil heater attached to a wall to generate a constant heat flux. O'Dowd et al. [8] applied this method on a transonic turbine blade tip. They found significant deviations between this method and others tested, which they attributed to non-uniform conduction into the blade tip resulting in an unknown thermal boundary condition. This demonstrated the common problem with steady state methods, which is that generating a known constant heat flux is difficult and measurements are often ill-conditioned.

Transient methods use measurements of the unsteady response of a wall to calculate heat transfer quantities. They are particularly well suited to short-duration facilities but have found wide ranging uses and are the main point of comparison to the new phase-based method presented in this paper. The most common technique applies a step change in flow temperature and measures the response of the wall temperature. Heat transfer coefficients are found by applying the governing equations of unsteady heat transfer. Early works fitted temperature measurements to the analytic solution for an ideal step change in flow temperature, however Schultz and Jones [9] explained that this leads to large errors as a true step change, as assumed by the theory, is unachievable in practice. An imperfect, non-instantaneous step can be approximated as a polynomial or as a superposition of many smaller steps, ramps or exponential functions [10]. Use of superposition with steps [11] and exponentials [12] is common when using thermochromic liquid crystals to detect discrete temperature intervals. Measurements of the time at which a temperature is reached, along with measurements of the flow temperature, are fit to analytic expressions for a semi-infinite surface through a regression procedure.

Another transient method reconstructs the heat flux into the wall. This can be done using a finite difference solution with measured wall temperatures applied as a boundary condition [13], however a more efficient method uses the impulse response technique developed by Oldfield [14]. This method generates a filter from the analytic impulse response of a 1D semi-infinite wall. Heat flux is calculated by applying the filter to the measured temperature response. O'Dowd et al. [8] showed that the impulse response method reduces processing time by a factor of 60 compared to a finite difference approach. Heat flux reconstructed from a transient measurement is used in a linear regression against wall temperature to calculate heat transfer coefficients. Playford [4] analysed uncertainty in transient measurements and identified three major sources: noise, modelling assumptions and the fit to analytic models due to the extent of the regression.

The effect of noise is to increase uncertainty in a regression as the minimised error remains high. For fixed instrumentation noise the impact on the wall temperature measurement is minimised by maximising the temperature difference being measured. The effect of noise on a regression can also be reduced by increasing the sample rate of the measurement, minimising uncertainty by statistical effects, however there are diminishing returns at high sample rates.

Uncertainty due to modelling assumptions arises as measurement methods assume the wall is 1D and semi-infinite such that the temperature response at any point is not affected by any temperature gradient on the measured surface or the other side (the "back-side") of the wall. The validity of these assumptions is determined by the Fourier number, Fo, given by

$$Fo = \frac{\alpha t}{L^2} \tag{2}$$

where α is the thermal diffusivity of the solid, t is the measurement time and L is the depth of the solid. Different interpretations of L are visualised in Fig. 2. Semi-infinite behaviour is limited by the depth into the wall at which the back-side boundary condition has an effect. An adiabatic boundary condition can arise when flows with similar heat transfer coefficients and adiabatic wall temperatures exist on either side of a solid, such as near the trailing edge of an aerofoil. In this case the midplane of the solid is approximately adiabatic and L is the depth to this midplane. Alternatively, if the flow on one side of a solid has a heat transfer coefficient much higher than on the other side, such as in an internal cooling channel, the wall where the heat transfer coefficient is high is approximately isothermal and L is the thickness of the wall. 1D behaviour is limited by the length scales over which lateral (2D or 3D) heat flux occurs. Lateral heat flux can arise due to a gradient in heat transfer coefficient on a flat surface, or due to a geometric feature in the surface. The length scale of lateral heat flux that limits 1D behaviour, and therefore the spatial resolution of the measurement, scales with the length scale of normal heat flux that limits semi-infinite behaviour, so the two can be considered analogous.

During a transient experiment the 1D, semi-infinite assumption gets progressively less accurate. There exists a Fourier number, Fo_{lim}, at which the errors in calculated heat transfer coefficients due to the breakdown of these assumptions becomes unacceptable. Schultz and Jones [9] suggested a value

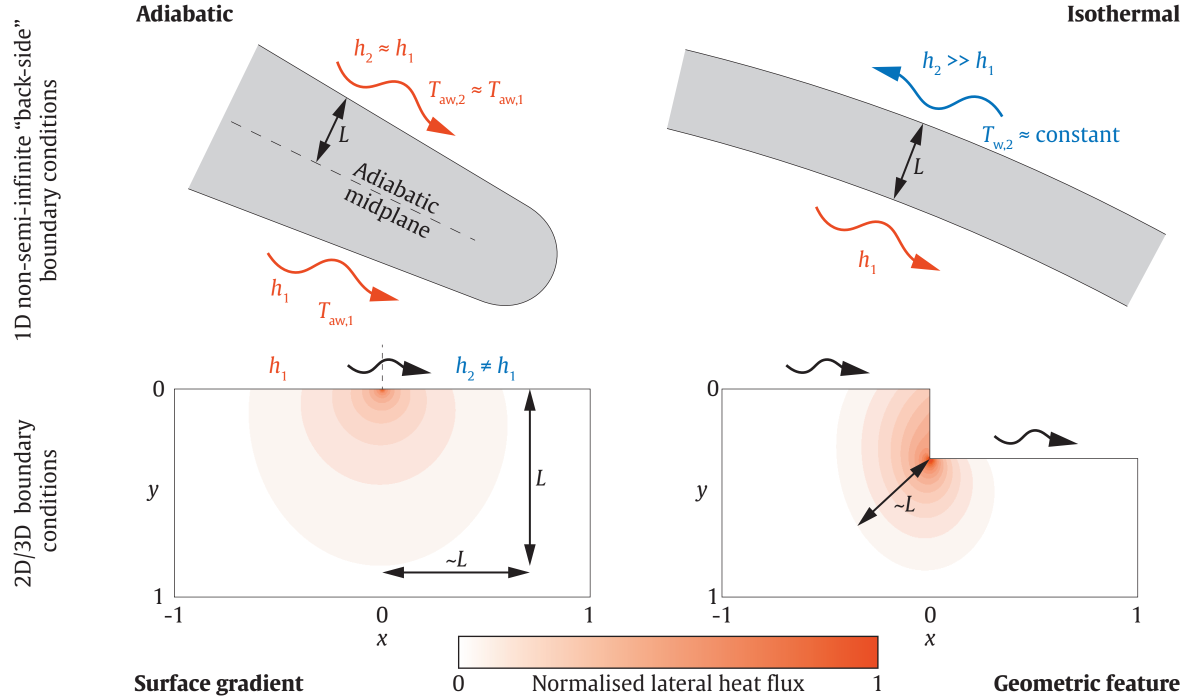

Figure 2 Non-ideal boundary conditions for 1D, semi-infinite modelling.

of $Fo_{\rm lim}$ = 0.1, a value also used by Thirumalai and Ekkad [15], while more conservative values of 0.075 and 0.0625 were suggested by Iliopoulou et al. [13] and Luque et al. [16] respectively. Playford [4] suggested a value of $Fo_{\rm lim}$ = 0.25 but noted that the optimal $Fo_{\rm lim}$ that minimises uncertainty depends on the experimental Biot number, the back-side thermal boundary condition and the presence of corners and surface curvature, which were shown by Wagner et al. [17] to reduce $Fo_{\rm lim}$. Analytical corrections for corners have been suggested [18], as have 3D reconstruction methods that apply measured temperatures to a numerical model [19]. Analytical methods remain limited by their assumptions while numerical reconstruction requires complete knowledge of the boundary conditions.

Uncertainty in calculating heat transfer coefficients by regression with analytic models is minimised by maximising the regression extent. Ideally the regression is performed using data from the moment the temperature step is applied to the time when the wall has reach equilibrium, however in reality this is not possible. A true step change to the flow temperature is unachievable due to the thermal mass of the experiment. Thermal mass is quantified with a time constant, the time taken for the flow temperature to rise by approximately 63 % of the final temperature change. Playford [4] suggested that when applying a linear regression with heat flux, any temperature samples from times within 5.5 time constants of the step should be removed from the regression. The floating regression method of Collins et al. [20] can correct for a time-varying temperature and allow more samples to be used, however there are always a number of samples that must be discarded. The end of the regression is set by $Fo_{\rm lim}$. If α/L^2, a property of the test piece, is small then a long time period can be used and the wall can achieve most of the maximum temperature change. Rotating rigs, such as a turbine, are limited in size and material choice by stress, power and aerodynamic similarity requirements. In these cases α/L^2 may be large and $Fo_{\rm lim}$ is reached before the wall has achieved more than a small amount of the maximum temperature change. The regression extent, and thus the uncertainty in heat transfer coefficient measurement, is limited by both the thermal time constant of the experiment and the time in which the semi-infinite assumption holds.

Current practice in measuring heat transfer coefficients experiences uncertainty because of noise in measurements and limits on the temperature change achievable between the time constant of heating and the Fourier number limit on measurement assumptions. For a given material and heat transfer coefficient, shorter length scales reach the limiting Fourier number first, limiting the regression extent and increasing the effect of noise on the calculated heat transfer coefficient. A larger input temperature change, and therefore more heating power, is then needed to reduce uncertainty. There is a need for a measurement method less sensitive to noise, meaning it doesn't require impractically large temperature changes.

2.2. *Phase-based measurements*

Several methods have been developed that use phase to measure heat transfer quantities in different flows and geometries. These methods are summarised here.

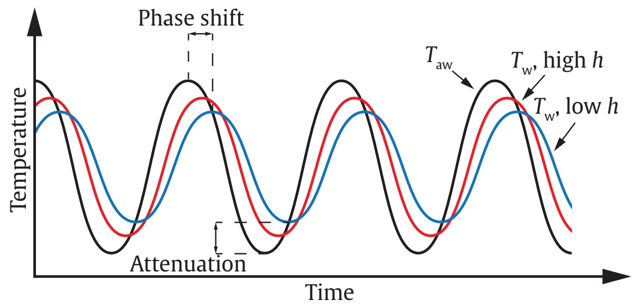

Figure 3 Illustration of the concept of phase-based heat transfer measurement.

The concept of using an oscillating fluid temperature to measure heat transfer coefficient is visualised in Fig. 3. Conduction and thermal inertia result in the wall temperature lagging behind the fluid temperature, measured as a phase-shift. The same effects also attenuate the amplitude of fluid temperature variation. The amount of phase-shift and attenuation depends on the heat transfer coefficient. As heat transfer coefficient increases there is less attenuation and phase-shift as the wall temperature reacts faster. This is the basis of the measurements discussed here.

Phase-shift and attenuation is affected by the material properties of the wall. Testing for these properties is a common use of phase-based measurements. One early example is from Ångström [21], who measured the thermal conductivity of metal bars by periodically heating them with steam. In modern use the technique is called lock-in thermography, where phase images of parts from periodic heating reveals sub-surface defects [22].

Significant work on phase-based methods has been done on thin-walled components that are not semi-infinite. Measuring the response of a wall to periodic heating allows heat transfer coefficients on the opposite side to be calculated. Roetzel et al. [23] demonstrated a method where points on the outer surface of an agitated vessel were pulsed with a laser and the temperature response measured with an IR camera, giving point measurements of internal heat transfer coefficients. Wandelt and Roetzel [24] and Freund [25] extended this by using laser sheets, allowing for full-field measurements of the surface. Röger [26] used an array of heat lamps on the outer surface of a dome with internal impinging jets, showing that a phase-based method has significant advantages over conventional measurements on curved surfaces.

When measuring heat transfer coefficients in a periodically heated pipe flow Roetzel [27] noted that, for a measurement signal that is proportional to temperature, no calibration is needed to calculate phase-shift. This removes a significant source of measurement uncertainty. Baughn et al. [28] and Leblay et al. [29] both used the attenuation of temperature amplitude, rather than phase-shift, to measure heat transfer coefficients. Baughn et al. [28] found that their results were affected by measurement noise, and other authors advise against using attenuation [23–25] for this reason. Attenuation can be used as a secondary measurement along with phase-shift. Roetzel et al. [30] used attenuation and phase-shift to calculate both heat transfer coefficient and a material property with one measurement.

In summary, past work on phase-based methods shows its potential as a measurement technique, with benefits in low sensitivity to noise and calibration. Most work has been done using radiative heating of non-semi-infinite parts. The next section develops the theory for phase-based measurements on 1D semi-infinite walls with periodically varying fluid temperature.

3. Phase-based measurement theory

In this section a derivation of the key results for a phase-based measurement is given. As with transient methods discussed in Section 2.1 this phase-based method assumes as semi-infinite wall is semi-infinite with 1D conduction. There are no additional assumptions, suggesting an equivalence between this new method and traditional transient methods. The flow has some adiabatic wall temperature $T_{\mathrm{aw}}(t)$ that varies in time t, with a constant heat transfer coefficient at the wall h. The wall takes a temperature $T_{\mathrm{w}}(t)$ and the solid, with uniform thermal diffusivity α and thermal conductivity λ, has a temperature distribution $T(y,t)$. The heat equation governs conduction in the solid

$$\frac{\partial T(y,t)}{\partial t} = \alpha \frac{\partial^2 T(y,t)}{\partial y^2} \tag{3}$$

subject to a convective boundary condition at the wall

$$-\lambda \left.\frac{\partial T(y,t)}{\partial y}\right|_{y=0} = h(T_{\mathrm{aw}}(t) - T_{\mathrm{w}}(t)) \tag{4}$$

A semi-infinite boundary condition and uniform initial temperature T_{i} gives

$$T(\infty,t) = T_{\mathrm{i}} \quad \text{(5a)} \qquad T(y,0) = T_{\mathrm{i}} \quad \text{(5b)}$$

A temperature difference relative to T_{i} is defined as

$$\Theta_{\mathrm{aw}}(t) = T_{\mathrm{aw}}(t) - T_{\mathrm{i}} \quad \text{(6a)} \qquad \Theta_{\mathrm{w}}(t) = T_{\mathrm{w}}(t) - T_{\mathrm{i}} \quad \text{(6b)}$$

Applying a Laplace transform and solving the resulting ordinary differential equation (see Appendix A) gives a transfer function between the wall and adiabatic wall temperatures

$$\frac{\widehat{\Theta}_{\mathrm{aw}}}{\widehat{\Theta}_{\mathrm{w}}} = 1 + \frac{e\sqrt{s}}{h} \tag{7}$$

where $e = \lambda/\sqrt{\alpha}$ is the thermal effusivity of the solid. In a phase-based measurement the adiabatic wall temperature is varied periodically. For a single angular frequency ω, the wall and adiabatic wall temperatures are sinusoids with amplitudes ΔT_{aw} and ΔT_{w} and phases ϕ_{aw} and ϕ_{w}, respectively. The steady state response of the wall is found by setting $s = j\omega$ in Eq. 7, where j is the imaginary unit. Taking the argument of the result gives a phase-shift $\phi = \phi_{\mathrm{aw}} - \phi_{\mathrm{w}}$ between the wall and adiabatic wall temperatures.

$$\phi = \arg\left(\frac{\widehat{\Theta}_{\mathrm{aw}}}{\widehat{\Theta}_{\mathrm{w}}}\right) = \arg\left(1 + \frac{e\sqrt{j\omega}}{h}\right) = \tan^{-1}\left(\frac{\frac{e}{h}\sqrt{\frac{\omega}{2}}}{1+\frac{e}{h}\sqrt{\frac{\omega}{2}}}\right) \tag{8}$$

Rearranging for the heat transfer coefficient gives

$$h = e\sqrt{\frac{\omega}{2}}\,(\cot\phi - 1) = e\sqrt{\pi f}\,(\cot\phi - 1) \tag{9}$$

where f is the frequency such that $1/(2f)$ is the half-period of oscillation. This expression turns a measurement of the phase-shift between fluid and wall temperatures into a measurement of the heat transfer coefficient. Equation 9 is non-dimensionalised by defining a Biot number $Bi = hL/\lambda$ and Fourier number $Fo = \alpha/(2fL^2)$

$$Bi = \sqrt{\frac{\pi}{2Fo}}\,(\cot\phi - 1) \tag{10}$$

The amplitude attenuation of the adiabatic wall temperature by the wall is found from the magnitude of Eq. 7 with $s = j\omega$. The non-dimensional result is

$$\left|\frac{\Delta T_{\mathrm{w}}}{\Delta T_{\mathrm{aw}}}\right| = \left[1 + \frac{\sqrt{2\pi}}{Bi\sqrt{Fo}} + \frac{\pi}{Bi^2 Fo}\right]^{-\frac{1}{2}} \tag{11}$$

Curves of Eq. 10 and Eq. 11 are shown in Fig. 4. Phase-shift and amplitude are plotted against $Bi\sqrt{Fo}$, a dimensionless group given by

$$Bi\sqrt{Fo} = \frac{h}{e\sqrt{2f}} \tag{12}$$

which is independent of length scale and is characteristic of convective heat transfer to a semi-infinite solid. The effects of heat transfer coefficient and frequency are seen in the phase and amplitude plots. As the heat transfer coefficient decreases, or the frequency increases, the phase-shift from the surface increases, up to the limit of 45°. The amount of attenuation increases as the heat transfer coefficient decreases or the frequency increases. The amount of attenuation sets the SNR of the wall temperature measurement, so the choice of frequency is limited by instrumentation sensitivity.

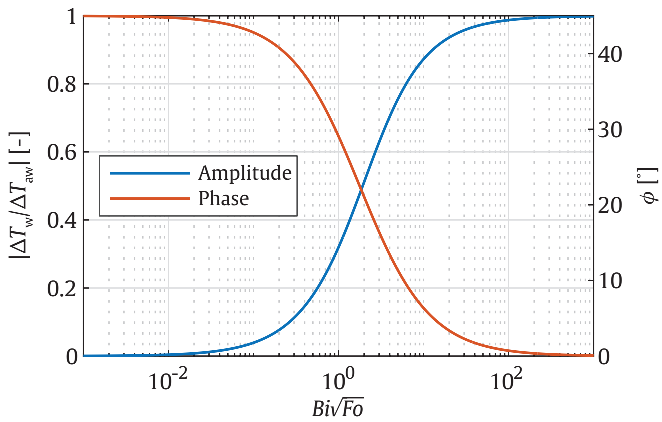

Figure 4 Variation in amplitude attenuation (left axis) and phase-shift (right axis) with $Bi\sqrt{Fo}$ for a 1D semi-infinite convective wall.

In a transient measurement, where the amplitude of the surface temperature is needed, noise directly changes the measured value, inducing error in a regression for heat transfer coefficient.

The effect of noise on a phase measurement is less obvious. In Appendix B it is shown that, for a noisy signal of a single frequency with true amplitude ΔT_{w}, noise amplitude ΔT_{n} and a uniformly distributed phase noise, the mean error in the measured phase due to noise is

$$\delta\phi_{\mathrm{mean}} = \frac{\Delta T_{\mathrm{n}}}{\Delta T_{\mathrm{w}}}\frac{2}{\pi} \approx \frac{\Delta T_{\mathrm{n}}}{\Delta T_{\mathrm{w}}} \times 36.5^{\circ} \tag{13}$$

The sensitivity of a measurement of heat transfer coefficient to phase error is found by differentiating Eq. 9 to get

$$\frac{\delta h}{h} = \frac{\delta\phi}{\sin^2\phi - \cos\phi\sin\phi} \tag{14}$$

Equation 14 is plotted in Fig. 5. For phase-shifts between 10° and 35° the relative error in heat transfer coefficient per degree of phase error is approximately 10 %, while outside that range the error is unbounded. This is because for phase-shifts $< 10°$ the phase error is a large fraction of the overall phase-shift, while at phase-shifts $> 35°$ the heat transfer coefficient is low, so any error in it is relatively large. For phase-shifts between 10° and 35° the ratio of noise amplitude to wall temperature amplitude should be less than 0.025 for uncertainty below 10 %. Comparing Fig. 5 to Fig. 4 shows that experiments should be designed to have $Bi\sqrt{Fo}$ around 1-5 to maximise wall temperature amplitude while keeping phase-shift above 10°.

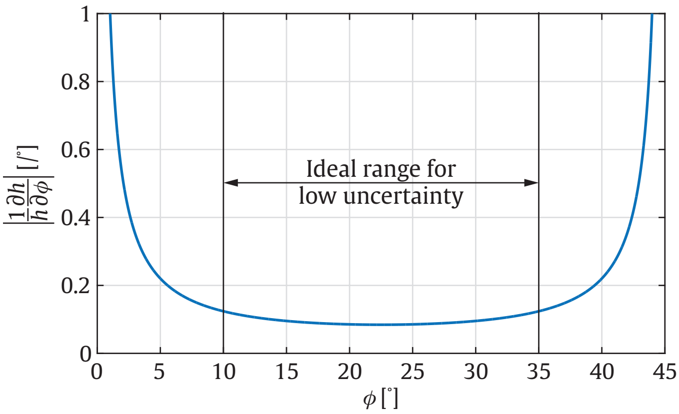

Figure 5 Relative error in heat transfer coefficient per degree of phase error across the range of possible phase-shifts.

Following the method in Appendix A gives transfer functions between the wall and adiabatic wall temperatures for non-semi-infinite walls. For either isothermal or adiabatic boundary conditions on the back-side these transfer functions are

$$\frac{\widehat{\Theta}_{\mathrm{aw}}}{\widehat{\Theta}_{\mathrm{w}}} = \begin{cases} 1 + \frac{e\sqrt{s}}{h}\left(\frac{1+\exp\left(-2\sqrt{\frac{s}{\alpha}}L\right)}{1-\exp\left(-2\sqrt{\frac{s}{\alpha}}L\right)}\right) & \text{Isothermal} \\ 1 + \frac{e\sqrt{s}}{h}\left(\frac{1-\exp\left(-2\sqrt{\frac{s}{\alpha}}L\right)}{1+\exp\left(-2\sqrt{\frac{s}{\alpha}}L\right)}\right) & \text{Adiabatic} \end{cases} \tag{15}$$

Setting the Laplace parameter $s = j\omega$ shows that the new terms in the exponential functions scale like

$$L\sqrt{\frac{j\omega}{\alpha}} \sim \frac{1}{\sqrt{Fo}} \tag{16}$$

These non-semi-infinite transfer functions tend to the semi-infinite transfer function in Eq. 7 in the limit of low Fourier number. This applies to both transient and oscillating temperature inputs, but demonstrates that with a phase-based method higher frequencies can be used to stay within semi-infinite Fourier number limits, within the limitations of SNR shown in Fig. 4.

Theory presented here shows why phase-shift can be used to measure heat transfer coefficients. The next section analyses the method numerically in comparison to a transient method.

4. Numerical analysis

This section presents a series of numerical experiments that develop signal processing procedures and analyse the phase-based method. Equivalent experiments are performed using a transient method and results are compared to demonstrate the benefits of the new method.

4.1. Numerical method and signal processing

Numerical experiments have been performed in MATLAB by generating wall temperature signals directly from transfer functions. To capture the effects of Fourier number on non-semi-infinite behaviour, the transfer functions in Eq. 15 were used, with an isothermal boundary condition applied unless stated otherwise. In phase-based measurements signals are generated from a Fourier series with the phase and magnitude of each harmonic found by setting $s = j\omega$. Transient measurement signals are generated by inverting the transfer functions using the concentrated matrix exponential method of Horváth et al. [31]. In a real experiment where the flow is only heated it is not possible to generate a zero-mean oscillation for a phase-based measurement, so there is a transient component to the signal not captured by a Fourier series. To compensate for this, signals in phase-based experiments have a transient component added, reflecting a step input with half the amplitude of the oscillation.

Input adiabatic wall temperatures are square waves for phase-based measurements and steps for transient. Square waves are convenient to generate experimentally, only requiring a heat source to be switched on and off with consistent timing, and have the benefit over a sinusoid of an infinite number of harmonics that can each be measured to provide redundant calculations of heat transfer coefficient at a range of Fourier numbers. The amplitude of higher harmonics drops off with $1/N$, so there is a limit to how many can be measured. For numerical experiments 25 square wave periods are generated, which is found to be sufficient for the idealised signals considered here.

In real experiments perfect square waves and steps are unachievable due to the thermal mass of the flow and heater. Realistic input adiabatic wall temperatures (i.e. flow temperatures) are generated by applying a first order time constant to the transfer functions. In a phase-based experiment the time constant acts to attenuate the amplitude of the temperature input, particularly for higher frequencies, placing a further limit on the use of high harmonics in practice. An example simulated square wave is shown in Fig. 6, demonstrating the rounding of the corner in the temperature rise due to the time constant.

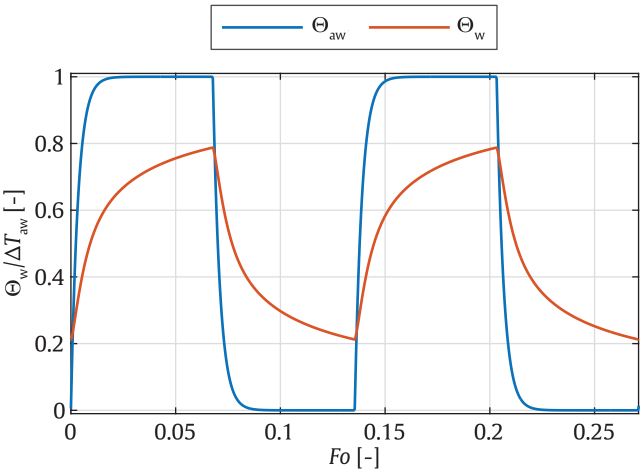

Figure 6 Example noise-less adiabatic and measured wall temperature signals for a phase-based measurement.

Generated temperature signals are processed with the same procedure as in a real experiment. For phase-based measurements the signal is high-pass filtered to remove the transient component of the signal without affecting the frequencies of interest. A 4th order Butterworth filter with a cutoff frequency at half the first harmonic is applied using the MATLAB function `filtfilt` for zero phase distortion. The signal is windowed with a Hann function to mitigate spectral leakage associated with a finite length signal with a possibly non-integer number of periods. A fast Fourier transform is applied to generate an amplitude spectrum from which the exact frequency of the harmonic of interest is found with a peak finding algorithm. While not necessary in controlled numerical experiments, this procedure is useful in real experiments to ensure the flow temperature has been oscillated at the expected frequency. The phase of the frequency of interest is found using a Goertzel discrete Fourier transform [32] at the relevant frequency index of the signal and taking the argument of the resulting complex number. The Goertzel algorithm is used for its efficiency at calculating discrete Fourier transforms for a small number of frequencies compared to a standard fast Fourier transform. In real experiments where a large number of signals may be analysed, such as from each pixel of an IR camera, this efficiency saves significant computational cost. Frequencies can be checked from the amplitude spectra of a single sample while the Goertzel algorithm is applied to all signals. This process of filtering, windowing and calculation of phase from the Goertzel discrete Fourier transform is applied to both the adiabatic and measured wall temperature signals. A heat transfer coefficient is then found by taking the phase-shift and applying Eq. 9 with the known frequency and material property.

For transient measurements the method of reconstructing heat flux and applying a linear regression is used with the signal processing method laid out by Playford [4]. Heat flux is calculated from the wall temperature using the impulse response method of Oldfield [14]. Heat transfer coefficients are then found using the floating regression method of Collins et al. [20] with a least squares method. The floating regression allows less data to be removed from the regression than the 5.5 time constant limit suggested by Playford [4]. It is found that for a noiseless signal a limit of 4 time constants can be used without increase in error. An example is shown in Fig. 7. Temperature data in Fig. 7a is processed to produce the heat flux data in Fig. 7b. The raw data shown in blue in Fig. 7b is without the floating regression method applied and shows a set of non-collinear points to the left of the figure where the adiabatic wall temperature has not reached a steady state and heat flux rises. The floating regression data shown in red uses measurements of the adiabatic wall temperature rise to normalise the measured wall temperature. This extends the linear region where a regression can be performed, shown in yellow, the gradient of which determines the heat transfer coefficient. The linear region is terminated when non-semi-infinite effects become significant due to the boundary conditions illustrated in Fig. 2. If the back-side boundary condition is isothermal the wall temperature levels off. Continuing the regression with this data results in an overestimate of the heat transfer coefficient. If the boundary condition is adiabatic the temperature rise until it reaches the adiabatic wall temperature. Using this data results in an underestimate of the heat transfer coefficient. If the wall remains

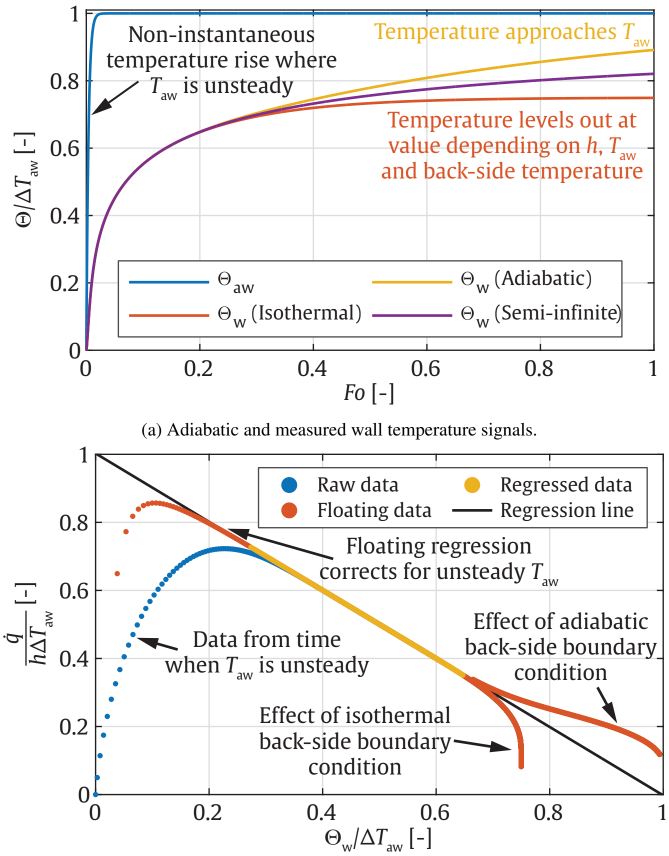

(a) Adiabatic and measured wall temperature signals.

(b) Calculated heat flux with a floating regression applied.

Figure 7 Example noise-less transient measurement showing the effects of different back-side boundary conditions.

semi-infinite then the data would continue to follow the black regression line, allowing for more data to be used in a low uncertainty regression.

Data for all signals is sampled uniformly in time. Errors in both transient and phase-based methods are a weak function of sample rate. In phase-based measurements the sampling rate must at minimum be greater than the Nyquist limit to resolve the frequency of interest. In all numerical experiments the sampling rate is at least 10 times greater than the point at which errors become significant for either method, typically 25 times or more than the forcing frequency for a phase-based measurement and high enough to give hundreds of points in a regression for transient measurements.

Artificial noise is drawn from a standard normal distribution. Different noise samples are added to adiabatic and measured wall temperatures before processing. Noise is scaled to the desired SNR, defined as the amplitude of the input adiabatic wall temperature to standard deviation of the noise.

4.2. Fourier number limits

Numerical experiments are performed over a range of Fourier and Biot numbers to assess the semi-infinite Fourier number limit for both phase-based and transient methods. To isolate non-semi-infinite effects the time constant is set to zero and SNR to infinity. Results are shown in Fig. 8. For both measurement methods errors grow fastest at low Biot numbers where conduction in the solid dominates over convective heat transfer. Errors with isothermal or adiabatic back-side boundary conditions are close to symmetric, as expected from the symmetry seen in Fig. 7b and Eq. 15. For phase-based measurements error in heat transfer coefficient swings from positive to negative as Fourier number increases, reflecting the behaviour of the argument of the transfer functions in Eq. 15. At the lowest Biot number of 0.1 error is greater than 5 % at a Fourier number of 0.1, while for larger Biot numbers error remains below 5 % until a Fourier number above 0.2. In transient measurements error grows monotonically as the regression can only go one way. For a Biot number of 0.1 error is below 5 % up to a Fourier number of 0.15, while for larger Biot numbers error is below 5 % up to Fourier numbers of 0.2-0.3.

In a real experiment Biot number may vary significantly, so the Fourier number limit is a compromise to minimise overall uncertainty. Indicated in Fig. 8 are values of $Fo_{\mathrm{lim}} = 0.1$ and $Fo_{\mathrm{lim}} = 0.2$ chosen for phase-based measurements and transient measurements, respectively. These values maximise Fo_{lim} while keeping the error at a Biot number of 0.1 below 5 %. The phase-based method is at a disadvantage as for the same experiment the lower Fo_{lim} reduces the wall temperature change that occurs while remaining semi-infinite. Depending on the heat transfer coefficient and material properties, halving Fo_{lim} from 0.2 to 0.1 reduces the wall temperature change by 2-30 %.

4.3. Effect of noise

To demonstrate how noise affects measurements a set of examples are shown. Figure 9 shows regressions from two transient numerical experiments with $Bi\sqrt{Fo_{\mathrm{lim}}} = 2$ and SNRs of

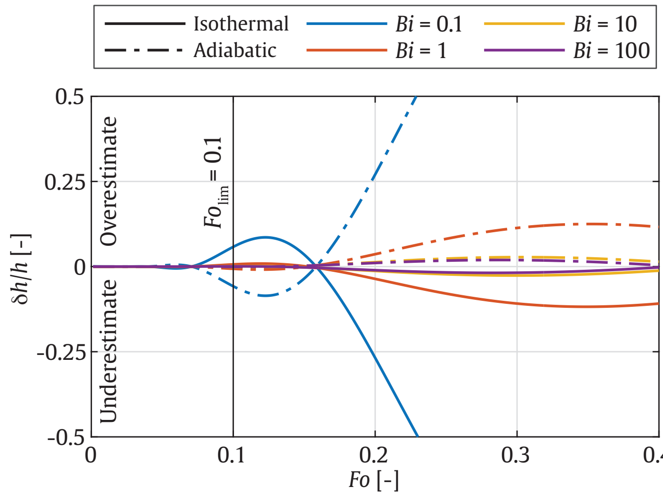

(a) Phase-based measurement.

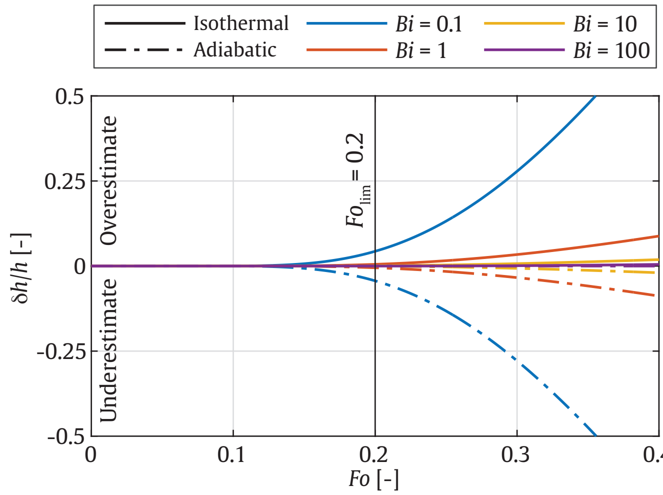

(b) Transient measurement.

Figure 8 Error in calculated heat transfer coefficient with varying Fourier number for phase-based and transient measurement methods. The back-side boundary condition is isothermal for solid lines and adiabatic for dashed lines.

1000 and 100. For an SNR of 1000 noise has a negligible effect on the regression, inducing an error in calculated heat transfer coefficient of 0.3 %. For an SNR of 100 the amplitude of the noise is large compared to wall temperature change, resulting in a regression error of 15.3 %. This example shows why transient experiments that measure temperature amplitude are sensitive to noise and need large temperature inputs for robust results.

Figure 10 shows amplitude spectra for measured wall temperature signals from phase-based numerical experiments performed with $Bi\sqrt{Fo_{\mathrm{lim}}} = 1.4$, reflecting the lower Fo_{lim} for phase-based experiments, and SNRs of 1000, 100 and 10. Noise is broadband and so even for an SNR of 10 the first harmonic in the wall temperature is 1000 times greater than the noise level. This ratio is 25 times greater than the limit for 10 % error given in Section 3. As a result, heat transfer coefficients measured with the phase-shift of the first harmonic have errors of 1.5 %, 0.3 % and 0.2 % respectively for SNRs of 10, 100 and 1000. An SNR of 1 is needed to produce error in the first harmonic above 10 %. Compared to a transient measurement, where an SNR of

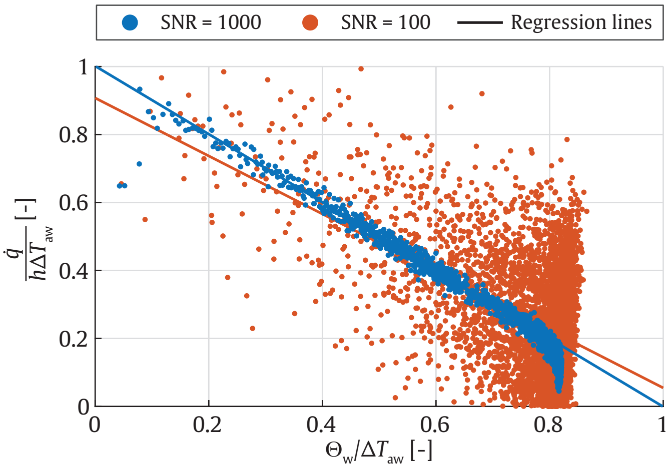

Figure 9 Transient measurement regressions at $Bi\sqrt{Fo_{\lim}} = 2$. For SNR = 100 and 1000, $|\delta h/h| = 15.3\,\%$ and 0.3 % respectively.

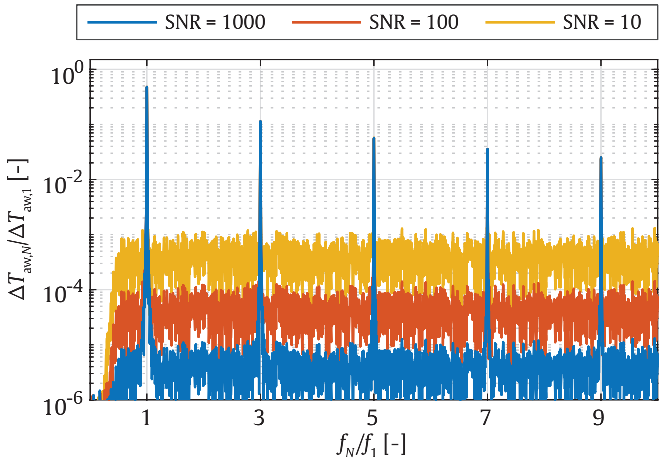

Figure 10 Amplitude spectra for measured wall temperature signals at $Bi\sqrt{Fo_{\lim}} = 1.4$ with three noise levels. For SNR = 10, 100 and 1000, $|\delta h/h| = 1.5\,\%, 0.3\,\%$ and 0.2 % respectively for the first harmonic.

100 produces error greater than 15 %, this shows that measuring phase, rather than amplitude, reduces sensitivity to noise by more than an order of magnitude.

Figure 10 shows the drop off in amplitude of higher harmonics, with the ninth harmonic in the wall temperature having an amplitude of 2.5 % of the first harmonic in the adiabatic wall temperature. This is due to a combination of the underlying Fourier series, the filtering effect of the time constant applied to the input adiabatic wall temperature and filtering by the semi-infinite surface. The attenuation of higher harmonics increases the uncertainty of heat transfer coefficient measurements made using them. For an SNR of 1000 all five harmonics plotted have error below 0.5 %, but for an SNR of 100 error is greater than 2 % for the third harmonic while for an SNR of 10 error is greater than 5 % for the third harmonic and 20 % for the fifth harmonic. This demonstrates that using higher harmonics, and higher frequencies in general, increases uncertainty in a phase-based measurement.

4.4. *Monte Carlo analysis*

Random noise produces non-deterministic errors that vary across the input space. To characterise average behaviour a statistical Monte Carlo method is used following the approach of Playford [4]. Numerical experiments are repeated a large number of times until statistical properties have converged, typically within 500 samples. The Monte Carlo analysis is performed by sweeping over SNR and $Bi\sqrt{Fo_{\lim}}$ to generate a 2D map. $Fo_{\lim}$ is fixed for each measurement method, so sweeping over $Bi\sqrt{Fo_{\lim}}$ is equivalent to sweeping over the Biot number alone. The value of $Bi\sqrt{Fo_{\lim}}$ is varied by holding heat transfer coefficient and thermal effusivity constant while changing the length scale L. With the length scale the time to end the regression in transient measurements and frequency in phase-based measurements is found. For each value of $Bi\sqrt{Fo_{\lim}}$ the thermal time constant applied to the input adiabatic wall temperature is set so that the value of $Bi\sqrt{Fo}$ relative to the time constant is 0.05.

Figure 11 shows results from Monte Carlo simulations with SNR varying from 0 to 1000. Contours of error in heat transfer coefficient are shown against Biot number, which is plotted rather than $Bi\sqrt{Fo_{\lim}}$ to allow for fair comparison between phase-based and transient methods. Results show that error increases at low Biot numbers for both methods, with Biot numbers less than 1 having error greater than 20 %. Above a Biot number of 2 the error is a weak function of Biot number. As seen in Fig. 9 a low SNR makes an accurate linear regression impossible. In transient measurements error grows quickly below an SNR of 400, with an SNR of 150 or less producing error greater than 10 %. In phase-based measurements error is less than 1 % for all values of SNR greater than 10 at a Biot number greater than 4, and error only grows above 10 % for SNR less than 3 or Biot numbers below 1. These results demonstrate the robustness of the phase-based method to noise.

With the results in Fig. 11 an experimentalist can determine the requirements for a successful heat transfer test. For a given flow and geometry, which sets the heat transfer coefficient and length scale, they should choose a material with minimum thermal effusivity and diffusivity to maximise $Bi\sqrt{Fo_{\lim}}$. For their chosen instrumentation, they can determine the temperature input needed for the SNR that gives acceptable error.

4.5. *Summary*

Numerical experiments in this section validate the theory of the new phase-based method and demonstrate its advantages. A semi-infinite Fourier number limit has been established and the effects of noise on phase-based and transient measurements have been discussed. A Monte Carlo analysis demonstrates the robustness of the new phase-based method to noise, allowing for the use of SNRs, and therefore experimental heat inputs, 10-100 times lower than required by a transient method. The results in this section are carried into the experimental methods described in the next section to validate the use of phase-based measurements on real test cases.

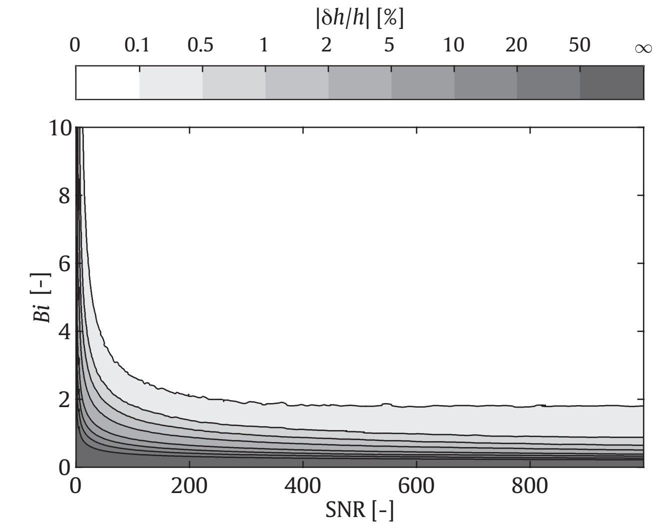

(a) Phase-based measurement.

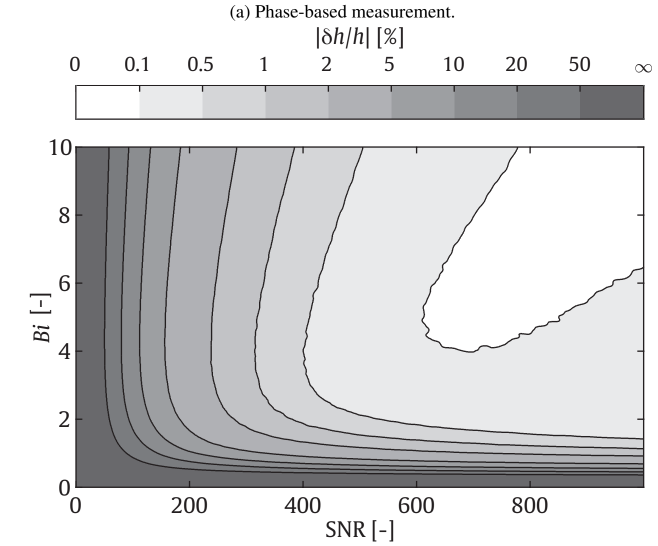

(b) Transient measurement.

Figure 11 Relative error in calculated heat transfer coefficient as a function of $Bi\sqrt{Fo_{\mathrm{lim}}}$ and SNR.

5. Experimental method

Experimental validation is required to show that the new phase-based method can be applied in practice. In this section the experimental method of phase-based measurements is described along with the methods used to validate and compare with the existing transient method.

5.1. Rig

A cross-section of the experimental rig is shown in Fig. 12. The wind tunnel is a draw-down configuration with atmospheric inlet and a water ring vacuum pump at the outlet. The inlet Mach number to the 45 mm × 45 mm working section is $M_\infty = 0.58$. The rig was designed for low uncertainty transient measurements by Hulhoven et al. [33] following the recommendations of Playford [4]. This allows for reference transient measurements to validate phase-based measurements. Two stainless steel heater meshes, designed following Ireland et al. [34], supply up to 15 kW of heat each to the inlet flow, together producing a temperature change up to 75 K. An 8.5:1 contraction leads to a turbulence grid generating a turbulence intensity of 4.8 %. The contraction and turbulence grid collar are designed for minimum volume and are manufactured from glass-filled polyamide, which is stable at high temperatures while minimising the thermal mass upstream of the working section. This minimises the thermal time constant of the temperature rise, measured to be 0.2 s. The working section side walls are sloped at 0.25° to compensate for boundary layer growth, generating a flow with less than 1 % acceleration from working section inlet to exit. One wall of the working section is a plate with test geometry machined on its surface. Bleed flow is extracted from the working section inlet, removing the inlet boundary layer and placing the stagnation point on the nose of the 7:1 ellipse that forms the leading edge of the plate. This results in a fresh boundary layer on the plate without a separation bubble. A pressure margin for bleed flow is provided by a throat downstream of the working section and bleed is controlled by ball valves. Previous results from the rig for heat transfer measurements and flow visualisation are shown by Hulhoven et al. [33] and Davis and Atkins [35].

Four plate geometries are tested. A flat plate provides a validation test to be compared with correlations and demonstrate the accuracy of heat transfer coefficient measurements. Three plates with forward and backward-facing steps and a vortex generator array are used as test cases that generate flow features of interest. Each plate is 235 mm long and 10 mm thick. The forward and backward-facing step plates have steps with height $H = 1.79$ mm, giving step Reynolds numbers $Re_H = 1.7 \times 10^4$ at a stream-wise Reynolds number $Re_x = 1 \times 10^6$. The vortex generator array plate has four evenly spaced vortex generators down the middle and two sets of half vortex generators at each side. The full vortex generator is 3.48 mm tall, 8.7 mm wide and 8.7 mm long. On each plate a minimally invasive boundary layer trip consisting of distributed silica beads, chosen following the method of Castillo Pardo et al. [36], is placed immediately downstream of the leading edge ellipse, 35 mm from the stagnation point at $Re_x = 0.3 \times 10^6$. This ensures a turbulent boundary layer is measured. Plates are machined from polycarbonate with measured thermal effusivity $e = 544\,\mathrm{J\,s^{-0.5}\,m^{-2}\,K^{-1}} \pm 2\,\%$ and thermal diffusivity $\alpha = 1.36 \times 10^{-7}\,\mathrm{m^2\,s^{-1}} \pm 4\,\%$ at 296.15 K. Both of these properties are functions of temperature, with e measured to change by approximately $1.37\,\mathrm{J\,s^{-0.5}\,m^{-2}\,K^{-1}}$ per Kelvin. This is a 1 % variation for temperature changes used in the phase-based method, but a greater than 10 % variation for temperature changes used in transient measurements. Theory does not account for variable material properties, so the small changes in the phase-based method minimise uncertainty due to material properties.

5.2. Instrumentation

A FLIR SC7300 IR camera measured full field wall temperatures on the test plates. The SC7300 is a cryogenically cooled camera with a resolution of 320×256 pixels, a spectral range of 7.7 µm-9.3 µm and a noise-equivalent temperature difference of

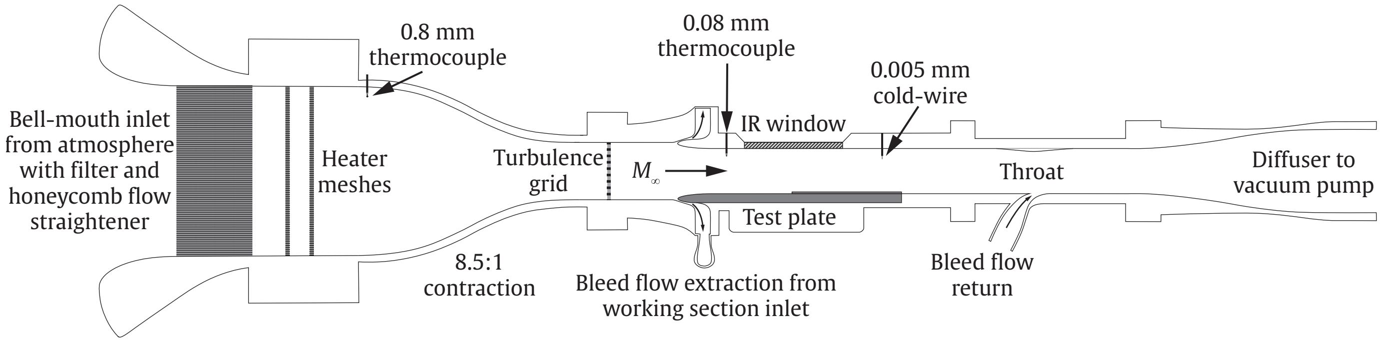

Figure 12 Cross section view of the experimental rig.

14 mK at an integration time of 320 µs. Videos of the wall temperature development are captured at 200 Hz. A multispectral grade zinc sulphide window in the wall opposite the test plate provides optical access to the working section. Two window positions are used to measure the full length of the flat plate downstream of the trip in separate tests. The camera and window are calibrated using a virtual black body. Each test plate and the walls of the test section are painted with matt black paint to give a surface emissivity of 0.94. The temperature of the window and aluminium test section walls are measured during experiments with type K thermocouples. This data is used to compensate for the radiosity of the walls and window when applying the camera calibration.

Flow temperature is measured with a 0.8 mm type K thermocouple (TC), a 0.08 mm type K TC and a 0.005 mm plated tungsten cold-wire (CW) thermometer. The cold-wire is a Dantec Dynamics 55P11 single-sensor miniature wire probe run as a resistance thermometer using the bridge circuit of Cho and Kim [37] with a low noise constant voltage supply and amplifier. Temperature accuracy, required to calculate gas properties, is achieved with the 0.8 mm and 0.08 mm TCs sampled at 100 Hz with a National Instruments 9214 module. To calculate heat transfer coefficients, a phase-shift $\phi = \phi_{aw} - \phi_w$ is needed. ϕ_w is found from IR camera recordings, but the phase of the heat input to the flow is unknown due to the thermal time constant, so ϕ_{aw} must be measured. A cold-wire is needed as the thermal mass of a temperature probe adds a phase-shift to the measurement. This phase-shift is estimated using the method of Dénos and Sieverding [38]. The Biot number relative to each probe is much less than one, so a lumped mass model is used with heat transfer coefficients estimated with correlations from Whitaker [39] to calculate a thermal time constant. Phase-shift is calculated by applying the time constant as a first-order filter. This model only accounts for the thermal mass of the thermocouple bead or tungsten wire and assumes that the lead wires or prongs can be neglected. Figure 13 shows results from the model, with the three probes compared at three Reynolds numbers relative to the diameter of the cold-wire. For experiments in this work $Re_{CW} \approx 10$. Phase-shift from the cold-wire is negligible at all three Reynolds numbers up to a frequency of 0.1 Hz, only reaching the level to produce a 5 % error above 1 Hz. A Dantec 55P11 probe used as a hot-wire in constant temperature anemometry has a bandwidth around 100 kHz, however the lack of a temperature control amplifier reduces the bandwidth when used as a cold-wire [40]. At 0.1 Hz and $Re_{CW} = 10$ a 0.08 mm TC adds a phase-shift of 0.8°, resulting in an error in heat transfer coefficient close to 10 %. The phase-shift of the 0.8 mm TC is unacceptably high for all frequencies of interest.

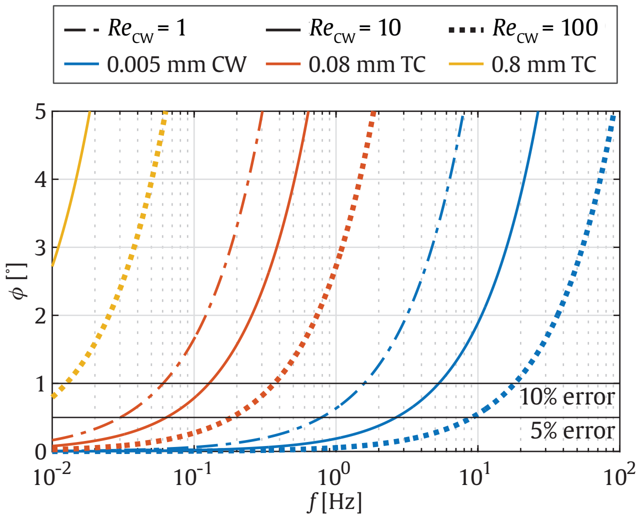

Figure 13 Instrumentation-induced phase-shift in flow temperature measurement at three Reynolds numbers relative to the diameter of the cold-wire probe.

To measure $\phi = \phi_{aw} - \phi_w$ the fluid and wall temperature measurements must be aligned in time to within 0.1 % of the oscillation period. This is achieved by sampling the cold-wire bridge voltage at 50 kHz and simultaneously triggering the IR camera from the same National Instruments USB-4431 module.

Figure 12 shows temperature probe locations. It is important that the probe used to measure ϕ_{aw} is positioned close to the measured surface in the stream-wise direction and away from any boundary layers or mixing that may add an additional phase-shift to the flow temperature. Static pressure is measured along the side wall and a pitot tube measures stagnation pressure, allowing for calculation of Mach and Reynolds numbers.

5.3. Data collection and processing

Unless otherwise stated, phase-based measurements used square wave inputs with a 5 s period and a 5 K amplitude, requiring a power input of 2 kW. Measurements were taken for

100 periods. A 5 s period gives values of $Bi\sqrt{Fo}$ around 2 for the expected heat transfer coefficients, which Fig. 4 and Fig. 5 show maximises the amplitude of the wall response while minimising error. A 5 s period gives a first harmonic Fourier number, Fo_1, of 0.0034 relative to the plate thickness and 0.11 relative to the step height, within the limits established in Section 4.2 for the expected Biot numbers.

Noise in experiments is uncontrollable and differs between the flow and wall temperature measurements. An SNR comparable to the numerical experiments is calculated to be $O(10)$ per Kelvin of temperature rise, giving phase-based measurements an SNR around 50. During a phase-based measurement Mach and Reynolds numbers in the working section vary by 0.1 % and 1 % respectively. Unsteadiness in the flow from heat input and due to physical processes such as vortex shedding is a source of noise, motivating the use of a low heat input.

A sample of data from a phase-based measurement is shown in Fig. 14. A trace of free stream temperature Θ_∞ is that what is measured by the cold-wire. Adiabatic wall temperature requires a recovery factor to be calculated, however it follows the free stream temperature instantaneously so there is no loss in accuracy from measuring the free stream temperature alone. Wall temperature traces are shown for three locations with different measured values of $Bi\sqrt{Fo}$. As expected from theory the amplitude of the wall response increases with $Bi\sqrt{Fo}$ and the shape changes as the phases of each harmonic shift. The amplitude response is also shown in the spectra in Fig. 14b, where it can be seen that the amplitude of higher harmonics drops off faster for the lower values of $Bi\sqrt{Fo}$.

Transient measurements used a reverse step input to match the Mach and Reynolds number of phase-based measurements. The flow is held at a high temperature until the rig is thermally soaked, at which time heating is lowered to the average temperature of the phase-based input. A 50 K temperature change is used, requiring a power input of 20 kW and giving an SNR of around 500. Data is collected for 45 s, corresponding to a Fourier number of 0.06 relative to the plate thickness and 1.91 relative to the step height. For the steps and vortex generators this is beyond the transient Fourier number limit, so data is removed from regressions, while for flat plate results where the limiting length scale is the thickness of the plate the whole data set can be used. Example data is shown in Fig. 15, where wall temperature traces are shown for the same three locations as

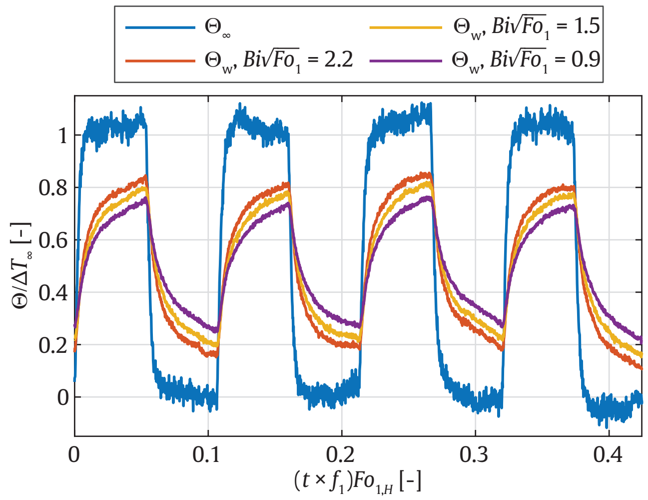

(a) Free stream and wall temperature signals.

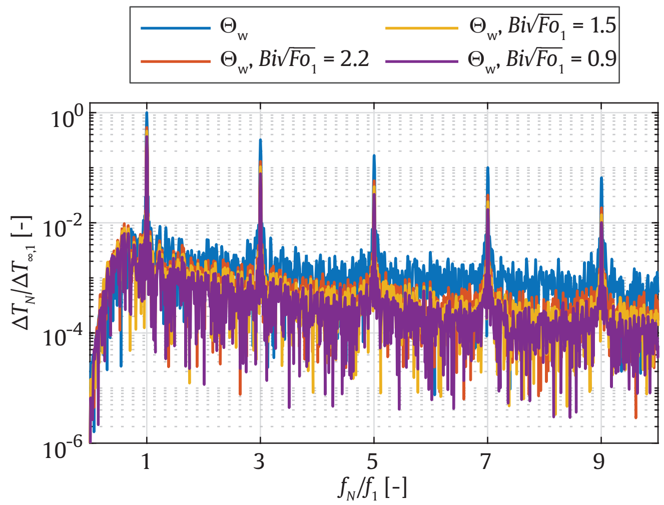

(b) Amplitude spectra for the four signals in (a).

Figure 14 Sample temperature signals and spectra showing free stream and wall temperatures from three pixels with different heat transfer coefficients.

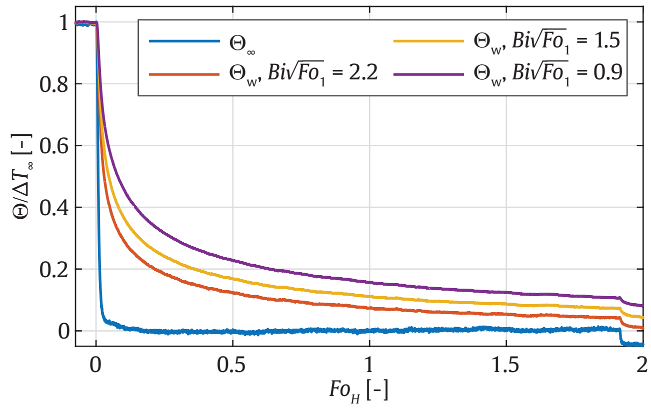

(a) Free stream and wall temperature signals.

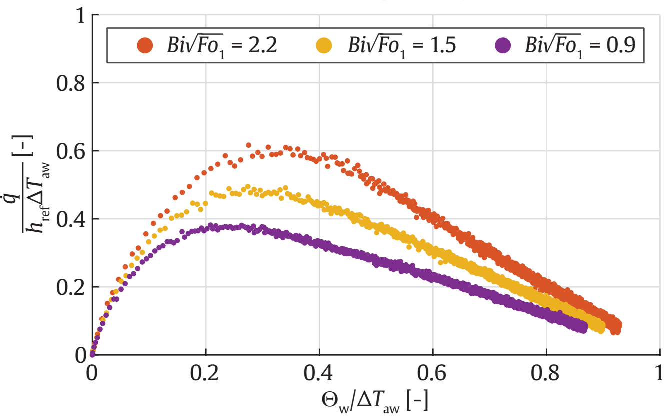

(b) Calculated heat flux for the three wall temperature signals in (a).

Figure 15 Sample temperature signals and calculated heat flux from three pixels with different heat transfer coefficients in a transient experiment.

data in Fig. 14 along with calculated heat flux data for use in regressions. The difference in noise level between transient and phase-based data can be seen, as can the different gradients in heat flux resulting from different heat transfer coefficients.

Data is processed in MATLAB using procedures outlined in Section 4.1. Full-frame IR videos produce 81 920 pixel signals. Optimisations such as windowing videos to a region of interest, parallel processing of pixel data and efficient memory allocation allows a full-field transient measurement to be processed in 30 s while phase-based processing takes 130 s using a modern 8 core CPU and 96GB of RAM. An average measured wall temperature is used to estimate the thermal properties of the polycarbonate and heat transfer coefficients are averaged over the central third of each plate to avoid corner flows.

6. Results

This section presents heat transfer coefficient results on the four plate geometries described in the previous section. Phase-based and transient measurements are compared to validate the new phase-based method.

6.1. Flat plate

Figure 16 shows flat plate results given as Nusselt number based on the length of the plate, Nu_L. Two Reynolds number ranges, labelled window 1 and window 2, indicate where measurements are collected for the two IR window positions required to view the full plate. Also plotted are correlations for laminar and turbulent boundary layers from Lienhard [41]. Two dashed lines show a range of ±15 %, which Lienhard [41] shows encloses 99.4 % of literature flat plate heat transfer data.

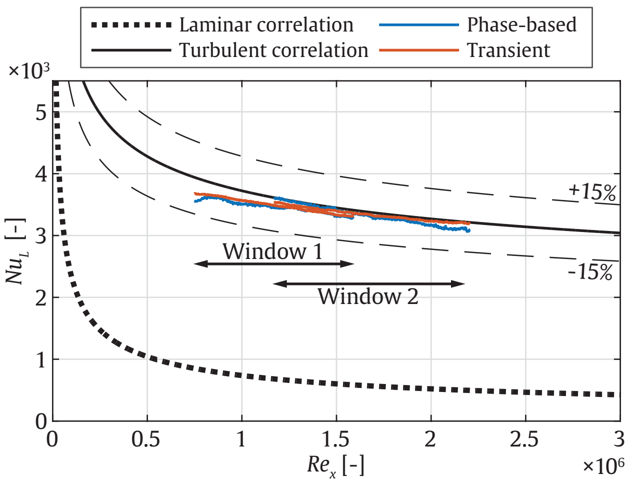

Figure 16 Flat plate Nusselt numbers measured with phase-based and transient methods. Data is compared to the correlation of Lienhard [41].

Results in Fig. 16 demonstrate that both phase-based and transient methods give accurate measurements. Phase-based and transient results from the same IR window position agree with a maximum difference of 2 %. The maximum run-to-run variation in the overlap region between the two window is 3 %. The maximum deviations from the correlation is 6 %, well within the 15 % variation seen by Lienhard [41]. The maximum deviation occurs at the furthest upstream point measured where the turbulent boundary layer is still developing after the trip.

6.2. Forward and backward-facing steps

Figure 17 shows backward and forward-facing step results given as Nusselt number based on the step height, Nu_H. Phase-based and transient methods agree away from the steps and capture the fall and rise in heat transfer as flow separates and reattaches over the steps. Peak transfer at reattachment is of particular interest as it leads to component failure [33]. Phase-based and transient results for peak Nu_H match within 3.3 % on the backward-facing step and 3.1 % on the forward-facing step.

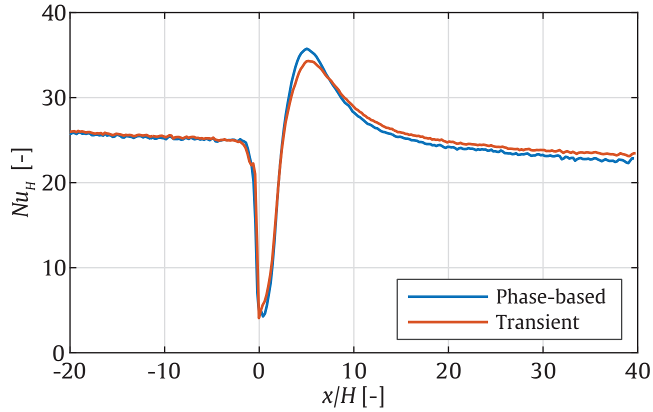

(a) Backward-facing step.

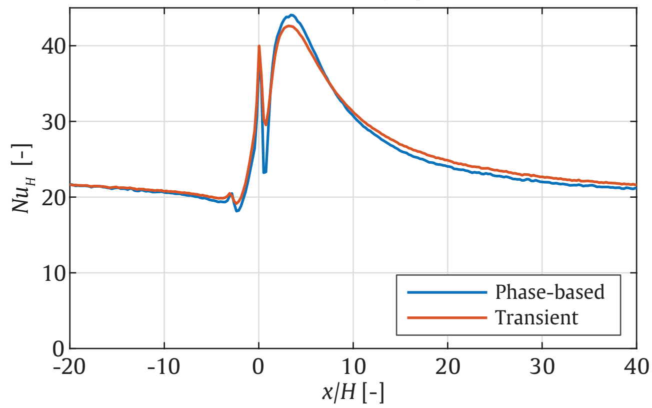

(b) Forward-facing step.

Figure 17 Nusselt numbers over backward and forward-facing steps measured with phase-based and transient methods.

To demonstrate the robustness to noise of the phase-based method measurements are taken on the forward-facing step with SNRs from 10-500, requiring heating power inputs from 0.4 kW-20 kW. Results are shown in Fig. 18. Phase-based results show maximum variation in peak Nu_H of 8 % between SNRs of 10 and 250. A variation of 6 % is expected between the highest and lowest SNRs due to Reynolds number variation between runs at different mean temperatures, leaving a 2 % variation due to measurement precision. The transient method measures the same peak Nu_H for SNRs of 250 and 500, however results from an SNR of 125 show deviations greater than 25 %, while results for SNRs of 50 and 25 are quite wrong, up to 100 % off.

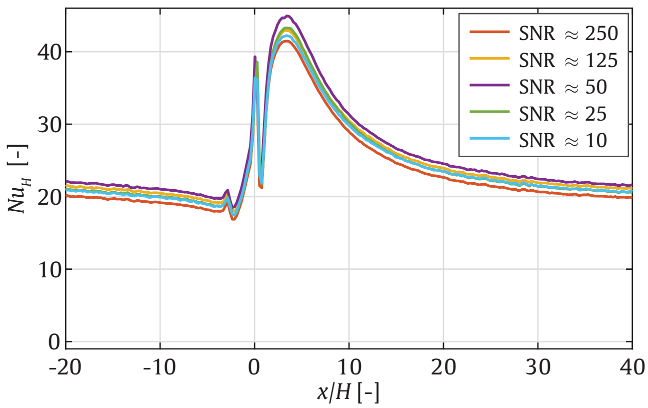

(a) Phase-based measurement.

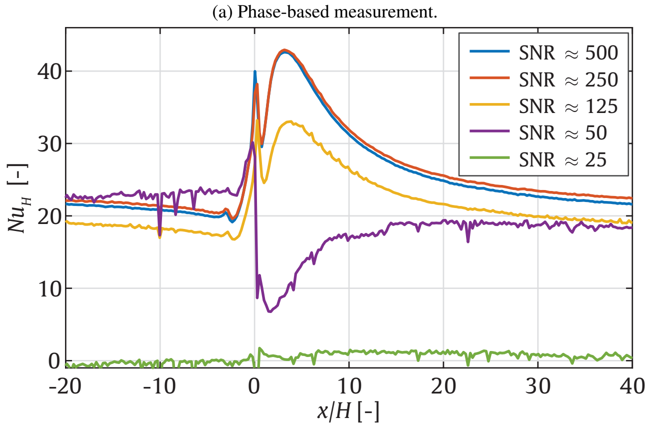

(b) Transient measurement.

Figure 18 Comparison of Nusselt number measurements over a forward-facing step with different SNRs for phase-based and transient measurements.

6.3. Vortex generator array

Figure 19 shows full-field results from the vortex generator array, given as Nusselt number based on the vortex generator height. The flow is symmetric down the centre line, so results are compared by mirroring the top half of the transient field.

Both methods showing the same level of heat transfer enhancement apart from at the tip of the vortex generators. The highest heat transfer coefficients are measured at the tips, with the transient measurement showing the region of high heat transfer extending down the vortex generators. The conduction length scale approaches zero at the tips where the three faces intersect, shortening the time during which the Fourier number is within semi-infinite limits. High heat transfer around the leading edge stagnation point means the back-side boundary condition is close to isothermal at the tip, so with any non-semi-infinite behaviour both methods would over-estimate heat transfer coefficient in this region.

In a phase-based measurement higher frequency harmonics with lower Fourier numbers can be used to measure regions where the first harmonic is beyond the semi-infinite limits. The drawback is that higher harmonics have lower amplitude and lower values of $Bi\sqrt{Fo}$, so uncertainty in resulting measurements of phase increases. To counteract this measurements from the first harmonic are used as a reference for higher harmonics. The phase of higher harmonics is adjusted to match heat transfer coefficient measurements with the first harmonic in regions where semi-infinite behaviour is maintained, such as the flat plate upstream the vortex generators. Regions where the first harmonic cannot be properly modelled as semi-infinite can then be interrogated. Figure 20 shows measurements of the second vortex generator using the fifth and ninth harmonics of the same measurement shown in Fig. 19. These measurements show that Nu_H at the tip is lower than measurements in Fig. 19 suggest. This is expected as flow separates over the sharp corner. Symmetric vortices are visible on the face of the vortex generator. These can be seen in Fig. 19 but at the Fourier numbers used lateral conduction blurs the measurement. With the higher harmonic frequencies the low heat transfer coefficients, and therefore low values of $Bi\sqrt{Fo}$, away from the vortex generators result in noisy measurements, particularly for the ninth harmonic, as expected.

6.4. Uncertainty analysis for cases with steps

Uncertainties for experimental results are given in Table 1 with maximum and mean values representative of measurements over the forward and backward-facing steps. Uncertainties are estimated using partial derivatives and the Monte Carlo analysis presented in Section 4.4. Contributions from the inputs to each method are given.

In transient measurements the dominant source of mean uncertainty is from the thermal properties of the material. The

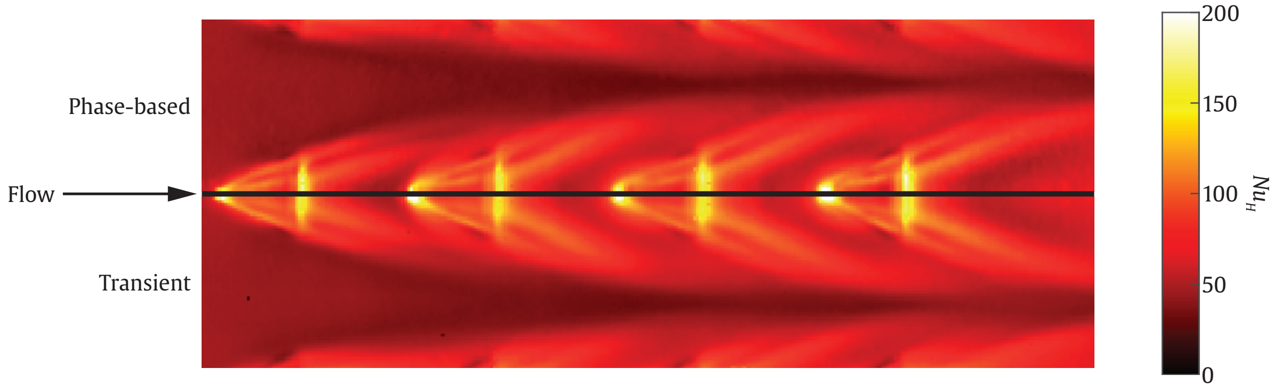

Figure 19 Nusselt number fields for the vortex generator array measured with phase-based and transient methods.

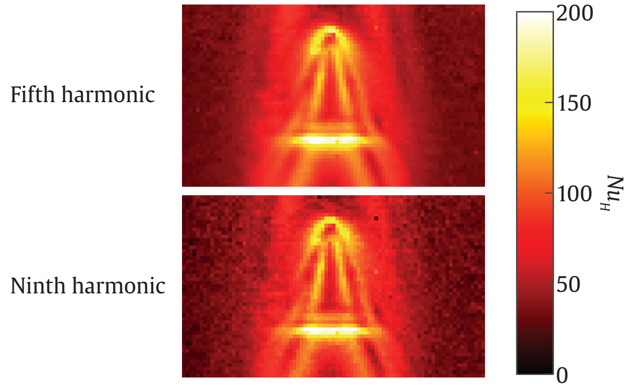

Figure 20 Nusselt number fields for the second vortex generator with the fifth and ninth harmonics of a phase-based measurement.

	Transient		Phase-based		
	Max.	Mean	Max.	Mean	
e	12.6	7.4	3.2	2.6	%
$\Theta_w/\Delta T_{aw}$	13.9	2.8	-	-	%
$\phi_{aw} - \phi_w$	-	-	11.2	5.7	%
f	-	-	0.1	0.1	%
Overall	28.2	10.4	14.9	8.6	%

Table 1 Uncertainty estimates for heat transfer coefficient measurements over forward and backward facing steps with contributions from each parameter.

polycarbonate was measured to an uncertainty of ±2 % but the variation of thermal effusivity with temperature and large temperature changes in transient measurements increase uncertainty. Maximum uncertainty in transient measurements is in the minimum heat transfer coefficient, resulting in low values of $Bi\sqrt{Fo}$ which make the measurement of $\Theta_w/\Delta T_{aw}$ sensitive to noise.

In phase-based measurements phase-shift is the dominant source of uncertainty. Uncertainty in phase-shift arises due to noise and the finite offset in time between free-stream and wall temperature measurements. Maximum uncertainty in phase-shift due to noise arises where $Bi\sqrt{Fo}$ is low, while the mean uncertainty is from the time offset. Temperature changes in phase-based measurements are 10 % of those used in transient measurements, so uncertainty in thermal effusivity is 25-30 % of that in transient measurements. The uncertainty contribution from the forcing frequency, is due to the finite resolution of the discrete Fourier transform. Overall, mean and maximum uncertainty in heat transfer coefficient is approximately 20 % and 50 % lower, respectively, than transient measurements.

7. Conclusions

This paper described a novel method for measuring heat transfer coefficients using the phase-shift between oscillating fluid and wall temperatures. A Laplace domain analysis of the unsteady heat equation with convective and semi-infinite boundary conditions produces a transfer function between fluid and wall temperatures. The steady-state frequency response shows that a measurement of phase-shift between fluid and wall temperatures is a measurement of heat transfer coefficient.

Previous work shows that transient methods require large temperature inputs due to sensitivity of measurements to noise. Minimising this sensitivity is limited by the need to use low enough Fourier numbers for conduction to remain semi-infinite.

Numerical experiments have established semi-infinite Fourier number limits for phase-based and a Monte Carlo analysis has shown that phase-based measurements are 10-50 times less sensitive to noise compared to transient measurements as the amplitude of broadband noise is orders of magnitude below the measured signal.

Experimental validation has demonstrated how the phase-based method can be applied in practice. Phase-based experiments require time-resolved measurements of fluid temperature for accurate phase-shift calculation. This is achieved with a cold-wire thermometer, while wall temperatures are measured with a high-speed infrared camera. Measurements on a flat plate, forward and backward-facing steps and a vortex generator array validate the accuracy of the phase-based method compared to correlations and an existing transient method. Phase-based measurements are achieved with signal-to-noise ratios, and therefore heating power inputs, 10-50 times lower than transient measurements. On geometries constrained by Fourier number limits, higher harmonics in a phase-based measurement can be used to probe areas where length scales are smallest.

Funding sources

This work was sponsored by Mitsubishi Heavy Industries and the Engineering and Physical Sciences Research Council (EPSRC reference EP/S023003/1).

Declaration of Competing Interest

The authors have no competing interests to declare.

CRediT authorship contribution statement

William Davis: Methodology, Software, Validation, Formal analysis, Investigation, Writing - Original Draft, Visualisation **Nicholas R. Atkins:** Conceptualisation, Supervision, Methodology, Resources, Writing - Review & Editing, Project administration, Funding acquisition.

Data availability

Data used in this paper is available upon reasonable request.

Acknowledgements

The authors thank Mitsubishi Heavy Industries for their generous financial support, with particular thanks to Yoshiyuki Okabe and Atsuya Sakata. Thanks also go to Dr Will Playford for early discussion of the work, to Dr Bram Hulhoven for the design and use of his heat transfer rig, and to Liam Cohen and Harry Agnew for their manufacturing work. The authors greatly appreciate their conversations with, and encouragement from, Prof. Nick Cumpsty, Colin Scrivener, Dr Tom Hynes and Prof. Tony Arts during the writing of this paper.

Appendix A. Transfer functions for a 1D surface

Picking up from Eq. 6 with $\Theta(y,t) = T(y,t) - T_{\mathrm{i}}$, the governing equations become

$$\frac{\partial\Theta(y,t)}{\partial t} = \alpha\frac{\partial^2\Theta(y,t)}{\partial y^2} \tag{A.1}$$

$$-\lambda\left.\frac{\partial\Theta(y,t)}{\partial y}\right|_{y=0} = h(\Theta_{\mathrm{aw}}(t) - \Theta_{\mathrm{w}}(t)) \tag{A.2}$$

Taking a Laplace transform of Eq. A.1

$$s\widehat{\Theta}(y,s) = \alpha\frac{\partial^2\widehat{\Theta}(y,s)}{\partial y^2} \tag{A.3}$$

where the initial condition $\Theta(y,0) = 0$ from Eq. 5b. The general solution to Eq. A.3 is

$$\widehat{\Theta}(y,s) = A\exp\left(-\sqrt{\frac{s}{\alpha}}y\right) + B\exp\left(\sqrt{\frac{s}{\alpha}}y\right) \tag{A.4}$$

Where A and B are constants. Setting $y = 0$, it follows that

$$\widehat{\Theta}_{\mathrm{w}}(s) = A + B \tag{A.5}$$

Taking a Laplace transform of Eq. A.2 and the derivative of Eq. A.4 gives

$$-\lambda\left.\frac{\partial\widehat{\Theta}(y,s)}{\partial y}\right|_{y=0} = h(\widehat{\Theta}_{\mathrm{aw}}(s) - \widehat{\Theta}_{\mathrm{w}}(s)) \tag{A.6a}$$

$$= -\lambda\sqrt{\frac{s}{\alpha}}(B - A) \tag{A.6b}$$

First applying the semi-infinite boundary condition from Eq. 5a, $\widehat{\Theta}(y,s)$ must be bounded in y, so $B = 0$ and $A = \widehat{\Theta}_{\mathrm{w}}(s)$.

$$\widehat{\Theta}(y,s) = \widehat{\Theta}_{\mathrm{w}}(s)\exp\left(-\sqrt{\frac{s}{\alpha}}y\right) \tag{A.7}$$

Substituting this result into Eq. A.6

$$\widehat{\Theta}_{\mathrm{w}}(s)\lambda\sqrt{\frac{s}{\alpha}} = h(\widehat{\Theta}_{\mathrm{aw}}(s) - \widehat{\Theta}_{\mathrm{w}}(s)) \tag{A.8}$$

Setting $e = \lambda/\sqrt{\alpha}$ and rearranging for transfer function between $\widehat{\Theta}_{\mathrm{w}}$ and $\widehat{\Theta}_{\mathrm{aw}}$ gives the result in Eq. 7.

$$\frac{\widehat{\Theta}_{\mathrm{aw}}}{\widehat{\Theta}_{\mathrm{w}}} = 1 + \frac{e\sqrt{s}}{h} \tag{A.9}$$

A non-semi-infinite boundary condition can be applied by considering the effect of a boundary condition at a depth L into the wall. The extremes of this are isothermal and an adiabatic conditions, given by Eq. A.10a and Eq. A.10b respectively

$$\Theta(L,t) = \Theta_L = 0 \quad \text{(A.10a)} \qquad \left.\frac{d\Theta(y,t)}{dy}\right|_{y=L} = 0 \quad \text{(A.10b)}$$

These boundary conditions take the same form when evaluated in the Laplace domain for $\widehat{\Theta}(y,s)$. Evaluating Eq. A.4 and its derivative at $y = L$ produces

$$\widehat{\Theta}_L(s) = A\exp\left(-\sqrt{\frac{s}{\alpha}}L\right) + B\exp\left(\sqrt{\frac{s}{\alpha}}L\right) \tag{A.11a}$$

$$\frac{d\widehat{\Theta}(L,s)}{dy} = \sqrt{\frac{s}{\alpha}}\left[B\exp\left(\sqrt{\frac{s}{\alpha}}L\right) - A\exp\left(-\sqrt{\frac{s}{\alpha}}L\right)\right] \tag{A.11b}$$

For the isothermal condition Eq. A.11a is set to zero. Substitution into Eqs. A.5 and A.6 gives the transfer function

$$\frac{\widehat{\Theta}_{\mathrm{aw}}}{\widehat{\Theta}_{\mathrm{w}}} = 1 + \frac{e\sqrt{s}}{h}\left[\frac{1+\exp\left(-2\sqrt{\frac{s}{\alpha}}L\right)}{1-\exp\left(-2\sqrt{\frac{s}{\alpha}}L\right)}\right] \tag{A.12}$$

For the adiabatic condition Eq. A.11b is instead set to zero and the transfer function is

$$\frac{\widehat{\Theta}_{\mathrm{aw}}}{\widehat{\Theta}_{\mathrm{w}}} = 1 + \frac{e\sqrt{s}}{h}\left[\frac{1-\exp\left(-2\sqrt{\frac{s}{\alpha}}L\right)}{1+\exp\left(-2\sqrt{\frac{s}{\alpha}}L\right)}\right] \tag{A.13}$$

Appendix B. Phase error due to noise

It is assumed that noise can be approximated as a Fourier series where at any frequency the noise has amplitude ΔT_{n} and phase ϕ_{n}. ΔT_{n} is a function of frequency. White noise has a constant ΔT_{n}, but any amplitude distribution is possible and may be set by unsteadiness in the flow or otherwise. ϕ_{n} is random with uniform distribution in the range $[0°, 360°)$. Expressing the periodically varying wall temperature in exponential form with noise at the same frequency gives

$$\Theta_{\mathrm{w}} = \Delta T_{\mathrm{w}}e^{j(\omega t+\phi_{\mathrm{w}})} + \Delta T_{\mathrm{n}}e^{j(\omega t+\phi_{\mathrm{n}})} \tag{B.1}$$

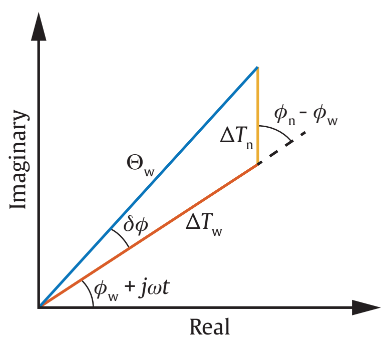

Figure B.21 Illustration of the effect of noise on a phase measurement at one frequency.

Equation B.1 is illustrated in an Argand diagram in Fig. B.21. The blue line Θ_{w} is the measured wall temperature signal, a combination of the true temperature in red and the noise in yellow. $\delta\phi$ is the error added to ϕ_{w}. $\delta\phi$ depends on the phase difference between the noise and wall temperature $\phi_\mathrm{n} - \phi_\mathrm{w}$ and the ratio of amplitudes $\Delta T_\mathrm{w}/\Delta T_\mathrm{n}$. Applying the law of sines to the triangle in Fig. B.21 and rearranging gives

$$\cot \delta\phi = \csc(\phi_\mathrm{n} - \phi_\mathrm{w}) \left(\frac{\Delta T_\mathrm{w}}{\Delta T_\mathrm{n}} + \cos(\phi_\mathrm{n} - \phi_\mathrm{w}) \right) \tag{B.2}$$

Normalised curves of Eq. B.2 are plotted in Fig. B.22. The magnitude of $\delta\phi$ is symmetric about 180°, so only the range $[0°, 180°)$ is shown. The curves converge as $\Delta T_\mathrm{w}/\Delta T_\mathrm{n}$ increases, approaching the function

$$\delta\phi = \arctan\left(\sin(\phi_\mathrm{n} - \phi_\mathrm{w}) \frac{\Delta T_\mathrm{n}}{\Delta T_\mathrm{w}} \right) \tag{B.3}$$

The limiting maximum phase error occurs when $\phi_\mathrm{n} - \phi_\mathrm{w} = 90°$ and is given by

$$\delta\phi_\mathrm{max} = \arctan\left(\frac{\Delta T_\mathrm{n}}{\Delta T_\mathrm{w}} \right) \tag{B.4a}$$

$$\approx \frac{\Delta T_\mathrm{n}}{\Delta T_\mathrm{w}} \approx \frac{\Delta T_\mathrm{n}}{\Delta T_\mathrm{w}} \times 57.3° \tag{B.4b}$$

If ϕ_n is uniformly distributed between 0° and 180° then the limiting mean of the phase error is

$$\delta\phi_\mathrm{mean} = \frac{1}{\pi} \int_0^\pi \delta\phi \,\mathrm{d}(\phi_\mathrm{n} - \phi_\mathrm{w}) \tag{B.5a}$$

$$= \frac{\Delta T_\mathrm{n}}{\Delta T_\mathrm{w}} \frac{2}{\pi} \approx \frac{\Delta T_\mathrm{n}}{\Delta T_\mathrm{w}} \times 36.5° \tag{B.5b}$$

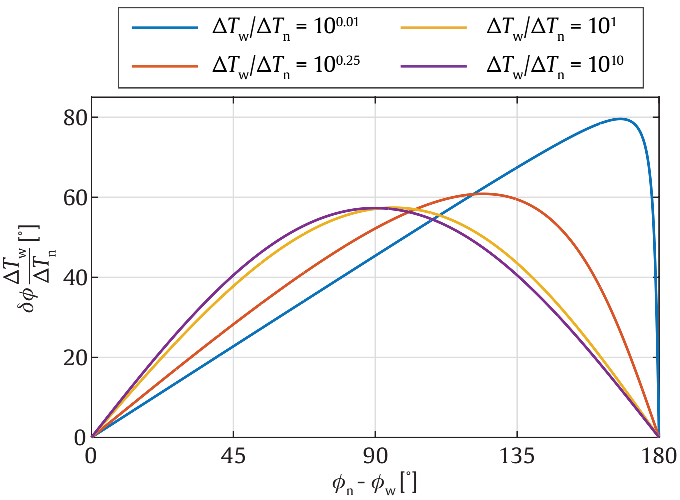

Figure B.22 Variation in phase error due to noise for different noise amplitudes and phase differences.

References

[1] R. J. Moffat, What's new in convective heat transfer?, International Journal of Heat and Fluid Flow 19 (2) (1998) 90–101. doi:10.1016/S0142-727X(97)10014-5.

[2] L. He, Spectral heat transfer coefficient for convection, International Journal of Heat and Mass Transfer 216 (2023). doi:10.1016/j.ijheatmasstransfer.2023.124557.

[3] J. M. Hacker, J. K. Eaton, Measurements of heat transfer in a separated and reattaching flow with spatially varying thermal boundary conditions, International Journal of Heat and Fluid Flow 18 (1) (1997) 131–141. doi:10.1016/S0142-727X(96)00142-7.

[4] W. Playford, Well-conditioned heat transfer measurements on engine scale gas turbine rigs, Ph.D. thesis, University of Cambridge (2018). doi:10.17863/CAM.22150.

[5] T. A. Moreira, A. R. A. Colmanetti, C. B. Tibiriçá, Heat transfer coefficient: a review of measurement techniques, Journal of the Brazilian Society of Mechanical Sciences and Engineering 41 (264) (2019). doi:10.1007/s40430-019-1763-2.

[6] P. Duda, Heat transfer coefficient distribution - a review of calculation methods, Energies 16 (9) (2023) 3683. doi:10.3390/en16093683.

[7] B. Laveau, R. S. Abhari, M. E. Crawford, E. Lutum, High resolution heat transfer measurement on flat and contoured endwalls in a linear cascade, Journal of Turbomachinery 135 (4) (2013) 041020. doi:10.1115/1.4007725.

[8] D. O. O'Dowd, Q. Zhang, L. He, P. M. Ligrani, S. Friedrichs, Comparison of heat transfer measurement techniques on a transonic turbine blade tip, Journal of Turbomachinery 133 (2) (2011) 021028. doi:10.1115/1.4001236.

[9] D. L. Schultz, T. V. Jones, Heat-transfer measurements in short-duration hypersonic facilities, AGARDograph 165, NATO Advisory Group for Aerospace Research and Development (1973).

[10] J. S. Kwak, Comparison of analytical and superposition solutions of the transient liquid crystal technique, Journal of Thermophysics and Heat Transfer 22 (2) (2008) 290–295. doi:10.2514/1.34274.

[11] S. V. Ekkad, J. C. Han, A transient liquid crystal thermography technique for gas turbine heat transfer measurements, Measurement Science and Technology 11 (2000) 957–968. doi:10.1088/0957-0233/11/7/312.

[12] D. R. H. Gillespie, S. M. Guo, Z. Wang, P. T. Ireland, S. T. Kohler, A comparison of full surface local heat transfer coefficient and flow field studies beneath sharp-edged and radiused entry impinging jets, in: ASME International Gas Turbine and Aeroengine Congress and Exhibition, Birmingham, UK, 1996, pp. 96–GT–428. doi:10.1115/96-GT-428.

[13] V. Iliopoulou, R. Deénos, N. Billiard, T. Arts, Time-averaged and time-resolved heat flux measurements on a turbine stator blade using two-layered thin-film gauges, Journal of Turbomachinery 126 (4) (2004) 570–577. doi:10.1115/1.1791647.

[14] M. L. G. Oldfield, Impulse response processing of transient heat transfer gauge signals, Journal of Turbomachinery 130 (2) (2008) 021023. doi:10.1115/1.2752188.

[15] M. P. Thirumalai, S. V. Ekkad, Effect of rotation on 45-degree borken v-ribs in a 2 pass square channel, in: ASME Turbo Expo: Turbine Technical Conference and Exposition, London, UK, 2024, pp. GT2024–128221.

[16] S. Luque, V. Kanjirakkad, I. Aslanidou, R. Lubbock, B. Rosic, S. Uchida, A new experimental facility to investigate combustor–turbine interactions in gas turbines with multiple can combustors, Journal of Engineering for Gas Turbines and Power 137 (5) (2015) 051503. doi:10.1115/1.4028714.

[17] G. Wagner, M. Kotulla, P. Ott, B. Weigand, J. Von Wolfersdorf, The transient liquid crystal technique: Influence of surface curvature and finite wall thickness, Journal of Turbomachinery 127 (1) (2005) 175–182. doi:10.1115/1.1811089.

[18] H. Jiang, W. Chen, Q. Zhang, L. He, Analytical-solution based corner correction for transient thermal measurement, Journal of Heat Transfer 137 (11) (2015) 111302. doi:10.1115/1.4030980.

[19] J. R. Ryley, M. McGilvray, D. R. H. Gillespie, Heat transfer coefficient determination on 3D geometries from transient thermochromic liquid crystal experiments, Journal of Thermophysics and Heat Transfer 33 (4) (2019) 1132–1141. doi:10.2514/1.T5701.

[20] M. Collins, K. Chana, T. Povey, Time-resolved heat transfer measurements, demonstrated on an unshrouded transonic turbine casing, Journal of Turbomachinery 138 (11) (2016) 111007. doi:10.1115/1.4033267.

[21] A. J. Ångström, New method of determining the thermal conductivity of bodies, The London, Edinburgh, and Dublin Philosophical Magazine and Journal of Science 25 (166) (1863) 130–142. doi:10.1080/14786446308643429.

[22] C. Meola, G. M. Carlomagno, A. Squillace, G. Giorleo, Non-destructive control of industrial materials by means of lock-in thermography, Measurement Science and Technology 13 (10) (2002) 1583–1590. doi:10.1088/0957-0233/13/10/311.

[23] W. Roetzel, S. Prinzen, M. Wandelt, Temperature oscillation technique for determination of local convective heat transfer coefficients without fluid temperature measurement, Chemical Engineering & Technology 16 (2) (1993) 89–93. doi:10.1002/ceat.270160204.

[24] M. Wandelt, W. Roetzel, Lock-in thermography as a measurement technique in heat transfer, in: Quantitative InfraRed Thermography 96 - Eurotherm Series 50, Pisa, Italy, 1997, pp. 189–194. doi:10.21611/qirt.1996.031.

[25] S. Freund, Local heat transfer coefficients measured with temperature oscillation IR thermography, Ph.D. thesis, Helmut-Schmidt-University (2008). doi:10.24405/353.

[26] M. Röger, A periodic-transient method for high-resolution heat transfer measurement on two-dimensional curved surfaces, Journal of Heat Transfer 129 (12) (2007) 1638–1654. doi:10.1115/1.2767677.

[27] W. Roetzel, Measurement of heat transfer coefficients in tubes by temperature oscillation analysis, Chemical Engineering & Technology 12 (1) (1989) 379–387. doi:10.1002/ceat.270120154.

[28] J. W. Baughn, J. E. Mayhew, M. R. Anderson, R. J. Butler, A periodic transient method using liquid crystals for the measurement of local heat transfer coefficients, Journal of Heat Transfer 120 (3) (1998) 772–777. doi:10.1115/1.2824349.

[29] P. Leblay, J.-F. Henry, D. Caron, D. Leducq, A. Bontemps, L. Fournaison, IR thermography measurement of convective coefficients in a pipe with periodic excitation, International Journal of Thermal Sciences 74 (2013) 183–189. doi:10.1016/j.ijthermalsci.2013.06.011.

[30] W. Roetzel, S. K. Das, X. Luo, Measurement of the heat transfer coefficient in plate heat exchangers using a temperature oscillation technique, International Journal of Heat and Mass Transfer 37 (1994) 325–331. doi:10.1016/0017-9310(94)90033-7.

[31] G. Horváth, I. Horváth, S. A.-D. Almousa, M. Telek, Numerical inverse laplace transformation using concentrated matrix exponential distributions, Performance Evaluation 137 (2020) 102067. doi:10.1016/j.peva.2019.102067.

[32] G. Goertzel, An algorithm for the evaluation of finite trigonometric series, The American Mathematical Monthly 65 (1) (1958) 34–35. doi:10.2307/2310304.

[33] B. Hulhoven, J. D. Coull, D. Jackson, N. R. Atkins, The impact of manufacturing variations on the aerothermal performance of high-pressure turbine blade shrouds, in: ASME Turbo Expo: Turbine Technical Conference and Exposition, London, UK, 2024, pp. GT2024–125688.

[34] P. T. Ireland, D. R. H. Gillespie, Z. Wang, Heating element, US Patent No. 6,181,874 B1 (2001).

[35] W. Davis, N. R. Atkins, Infrared thermography techniques for boundary layer state visualisation, Experiments in Fluids 65 (91) (2024). doi:10.1007/s00348-024-03827-8.

[36] A. Castillo Pardo, T. S. Williams, C. J. Clark, N. R. Atkins, C. A. Hall, M. J. Wilson, R. Vazquez Diaz, Boundary layer control for low reynolds number fan rig testing, Journal of the Global Power and Propulsion Society 7 (2022) 30–42. doi:10.33737/jgpps/158035.

[37] J. R. Cho, K. C. Kim, A simple high-performance cold-wire thermometer, Measurement Science and Technology 4 (12) (1993) 1346–1349. doi:10.1088/0957-0233/4/12/006.

[38] R. Dénos, C. H. Sieverding, Assessment of the cold-wire resistance thermometer for high-speed turbomachinery applications, Journal of Turbomachinery 119 (1) (1997) 140–148. doi:10.1115/1.2841002.

[39] S. Whitaker, Forced convection heat transfer correlations for flow in pipes, past flat plates, single cylinders, single spheres, and for flow in packed beds and tube bundles, AIChE Journal 18 (2) (1972) 361–371. doi:10.1002/aic.690180219.

[40] H. H. Bruun, Hot-Wire Anemometry: Principles and Signal Analysis, Oxford University Press, Oxford, UK, 1995. doi:10.1093/oso/9780198563426.001.0001.

[41] J. H. Lienhard V, Heat transfer in flat-plate boundary layers: A correlation for laminar, transitional, and turbulent flow, Journal of Heat Transfer 142 (6) (2020) 061805. doi:10.1115/1.4046795.